Green Chemistry

PAPER

View Article Online
View Journal | View Issue

Check for updates

Cite this: *Green Chem.*, 2026, **28**, 225

Rapid proton transport through a bio-inspired PO_4-built protective layer for stabilizing 5-hydroxymethylfurfural conversion at high current densities

Wei Ji,[a] Wenjie Zhang,[a] Chen Deng, *[b,c] Yuwei Xiong,[b] Qi Hao, [d] Hao Zhang, [e] Bing Song, [f] Wenlei Zhu, [g] Dekui Shen, [a] Jason Chun-Ho Lam *[h] and Richen Lin *[a]

Received 13th August 2025,
Accepted 21st November 2025

DOI: 10.1039/d5gc04249f

rsc.li/greenchem

Nickel-based electrocatalysts are pivotal for converting biomass-derived 5-hydroxymethylfurfural to 2,5-furandicarboxylic acid (FDCA), a key renewable precursor for biopolymers. However, their industrial adoption is limited by sluggish proton transfer kinetics, which restricts current density (targeting ≥200 mA cm^{-2}) and triggers catalyst corrosion *via* proton accumulation, reducing stability. Inspired by biological phosphate buffers that regulate protons to stabilize intracellular pH, we engineered a phosphate-built protective layer (PO_4-BPL) on a CuNiO catalyst. The PO_4-BPL serves dual roles: creating rapid proton channels to enhance proton-coupled electron transfer and protecting the catalyst from proton-induced corrosion. The PO_4-BPL/CuNiO delivers a current density exceeding 700 mA cm^{-2} with FDCA faradaic efficiency above 90% over 36 cycles, showcasing 7-fold stability improvement *versus* unmodified catalysts. In a continuous-flow electrolyzer, PO_4-BPL/CuNiO operates for 70 h, far exceeding the 6 h lifetime of the CuNiO. Density functional theory calculations confirm PO_4-BPL lowers proton migration energy barriers, enhancing mass transfer and preventing structural damage. This biomimetic strategy not only enables robust electrocatalysts for high current density applications, but also represents a green advance toward the sustainable and efficient production of biopolymer precursors.

Green foundation

1. This work advances green chemistry by developing a bio-inspired PO_4-built protective layer (PO_4-BPL) for electrocatalytic upgrading of biomass-derived 5-hydroxymethylfurfural (HMF) to 2,5-furandicarboxylic acid (FDCA), a key precursor for biodegradable plastics. The approach reduces dependency on fossil-based feedstocks and mitigates environmental impact by offering a sustainable and efficient alternative for biomass valorization.

2. This work achieves a breakthrough in green chemistry by enabling industrial-scale electrocatalytic conversion of biomass to bioplastics. **Quantitatively**, our bio-inspired PO_4-BPL on CuNiO: (1) boosts current density to >700 mA cm^{-2}; (2) maintained >90% FDCA selectivity over 36 stabilization cycles and improved catalyst stability by a 7-fold compared to no PO_4-BPL. In a continuous-flow electrolyzer, PO_4-BPL/CuNiO operates for 70 h, far exceeding the 6 h lifetime of the CuNiO. **Qualitatively**, PO_4-BPL solves proton transfer bottlenecks by mimicking biological buffers-accelerating proton-coupled electron transfer while preventing corrosion. Consequently, our work provides an energy-efficient and green electrochemical route to FDCA, enabling the replacement of fossil-derived terephthalic acid in plastic production and advancing the sustainable electrosynthesis of biopolymers for a circular bio-economy.

3. The biomimetic PO_4-BPL strategy shows promise beyond HMF-to-FDCA conversion. Research should actively explore its application to stabilize other critical biomass electro-oxidation reactions (*e.g.*, glycerol, sorbitol, lignin derivatives) at high current densities. Successfully adapting the protective layer concept to different substrate-catalyst systems would broaden the platform's impact, enabling the sustainable production of a wider array of renewable chemicals and fuels from diverse biomass sources, displacing more fossil-derived equivalents.

[a]*Key Laboratory of Energy Thermal Conversion and Control of Ministry of Education, School of Energy and Environment, Southeast University, Nanjing 211189, China. E-mail: richenlin@seu.edu.cn*
[b]*School of Chemistry and Chemical Engineering, Southeast University, Nanjing 211189, China*
[c]*Department of Electrical Engineering and Electronics, University of Liverpool, Liverpool L69 3GJ, UK. E-mail: chen.deng2@liverpool.ac.uk*
[d]*Key Laboratory of Quantum Materials and Devices of Ministry of Education, School of Physics, Southeast University, Nanjing 211189, China*
[e]*State Key Laboratory of Clean Energy Utilization, Zhejiang University, Hangzhou 310027, China*
[f]*Bioeconomy Science Institute, Titokorangi Drive, Private Bag 3020, Rotorua 3046, New Zealand*
[g]*State Key Laboratory of Water Pollution Control and Green Resource Recycling, School of the Environment, Nanjing University, Nanjing 210023, China*
[h]*School of Energy and Environment, City University of Hong Kong, Kowloon Tong, Hong Kong SAR, 999077, China. E-mail: jason.lam@cityu.edu.hk*

Published on 21 November 2025. Downloaded on 5/17/2026 11:33:50 AM.

Published on 21 November 2025. Downloaded on 5/17/2026 11:33:50 AM.

1. Introduction

Biomass-derived 2,5-furan dicarboxylic acid (FDCA), a renewable substitute for petroleum-derived terephthalic acid, represents a major green advance in decarbonizing industries reliant on plastics and energy materials.[1–4] With a projected market value exceeding $1.2 billion by 2030, FDCA-based polyethylene 2,5-furandicarboxylate exhibits 60% superior oxygen barrier properties over polyethylene terephthalate, enabling green sustainable packaging and high-performance battery separators to extend lithium-ion battery lifespans by >20%.[5–7] Conventional thermochemical FDCA synthesis, reliant on energy-intensive processes (90–140 °C, 0.1–4 MPa O_2) and noble oxidants (*e.g.*, Pt, Au, Ru), generates 10%–30% of byproducts in products, hindering scalability.[8–10] Electrochemical oxidation using renewable electricity offers a green alternative,[11–14] yet achieving industrial current densities ($\geq$200 mA cm^{-2}) remains challenging due to proton transfer inefficiencies and catalyst corrosion. Addressing these limitations requires innovative strategies to synchronize proton–electron transfer kinetics and stabilize catalytic interfaces, key to advancing green FDCA electrosynthesis for scalable biopolymer production.

Compared to noble metal catalysts, nickel-based electrocatalysts, distinguished by their favorable electron configuration and d-orbital hybridization,[15–17] excel in stabilizing transition metal–oxygen covalent bonds,[18–21] rendering them highly effective for 5-hydroxymethylfurfural (HMF) oxidation to FDCA *via* proton-coupled electron transfer (PCET) mechanisms. During electrocatalysis, *in situ* surface reconstruction generates active Ni^{III}–OOH species that mediate HMF dehydrogenation through sequential PCET steps, accompanied by Ni^{3+}/Ni^{2+} redox cycling (Scheme 1a).[22,23] While existing studies report FDCA faradaic efficiencies exceeding 90%, achieving industrial-grade current densities under alkaline conditions remains elusive due to kinetic bottlenecks in HMF-electrocatalyst interfacial mass transfer and proton diffusion.[24] Current systems typically operate below 200 mA cm^{-2}, primarily constrained by sluggish proton replenishment at high current densities, which exacerbates catalyst passivation and competitive oxygen evolution reaction (OER). Addressing these limitations necessitates interfacial engineering strategies to synchronize HMF adsorption, proton transfer kinetics, and active site architectures critical for balancing efficiency, stability, and scalability in practical electrocatalytic reactors.

How do biological organisms in nature regulate proton delivery and balance? Nature's phosphate buffer system, which dynamically regulates intracellular pH *via* $HPO_4^{2-}/H_2PO_4^-$ interconversion to stabilize proton activity during metabolic processes, offers a biomimetic blueprint for optimizing interfacial PCET microenvironments (Scheme 1b). In electrocatalysis, analogous strategies have been explored in OER/HER/hydrogenation of furfural systems, where surface-bound inorganic anions (*e.g.*, NO_3^-, SO_4^{2-}, CO_3^{2-}, PO_4^{3-}) modulate proton transfer kinetics and stabilize catalytic interfaces.[25–29] Previous studies on the molecular-level PO_4 groups modified on the perovskite oxide surface are a key factor in overcoming kinetic limitations of proton transfer in OER.[30] Hollow nanospheres catalyst of CoO_x–PO_4 with self-built phosphate film could effectively block chloride anions and implement robust seawater oxidation.[31] During the electrocatalytic conversion of HMF to FDCA, two distinct pathways emerge based on the system's pH level, with both pathways involving 6 e^- and 6 H^+ transfer steps (Scheme 1c). Proton transfer in electrocatalytic HMF conversion is a critical step, and the reaction can be significantly hindered if the proton transfer is blocked.[32,33] However, such anion-mediated interfacial engineering to enhance proton transfer remains underexplored in HMF oxidation, particularly in achieving a balance between high current density and long-term stability. Although Cu doping has shown promise in suppressing OER competition during HMF oxidation,[34,35] its role in tailoring active site electronic states and ensuring compatibility with phosphate buffer requires further investigation. Bridging these knowledge gaps through synergistic integration of bioinspired proton management, anion-modulated surface reconstruction, and alloying effects could unlock robust electrocatalytic systems capable of sustaining industrial current densities while minimizing energy and material costs.

Herein, inspired by natural phosphate-buffering mechanisms that regulate intracellular proton homeostasis, we constructed a green and safe biomimetic phosphate-built protective layer (PO_4-BPL) on CuNiO catalysts through hydrothermal phosphorylation, providing an eco-friendly alternative to conventional strategies that rely on complex organic ligands or toxic components. To standardize catalyst labels in this work, we named the thin film obtained by electrodeposition as CuNiO, the thin film containing PO_4-BPL after hydrothermal phosphating as PO_4-BPL/CuNiO (the layer comprises various phosphate species rather than solely PO_4^{3-}), and the phosphate-treated Cu-free film as PO_4-BPL/NiO. This dual-functional interface synergistically accelerates PCET kinetics during HMF oxidation whilst buffering interfacial pH to mitigate catalyst corrosion – a key green functionality (Scheme 1d). The incorporation of Cu dopants further modulates the electronic structure of Ni active sites, lowering the energy barrier for HMF dehydrogenation. Remarkably, the PO_4-BPL/CuNiO catalyst achieves industrial-grade current densities (>700 mA cm^{-2}) with near-unity FDCA selectivity across a wide potential window, outperforming conventional alkaline HMF oxidation systems by 7-fold in operational stability – a major green advance in process chemistry. By endowing the catalyst with "green longevity", this strategy significantly reduces chemical consumption and waste, moving beyond the conventional paradigm focused solely on high activity. Operando spectroscopic and computational analyses reveal that PO_4-BPL not only stabilizes the catalytically active $Ni^{III}OOH$ species but also establishes proton-relay channels to prevent surface proton accumulation. This bioinspired interfacial engineering strategy offers a green pathway to resolving the longstanding trade-off between high-current operation and catalyst durability in biomass electrorefining systems.

 This journal is © The Royal Society of Chemistry 2026

Published on 21 November 2025. Downloaded on 5/17/2026 11:33:50 AM.

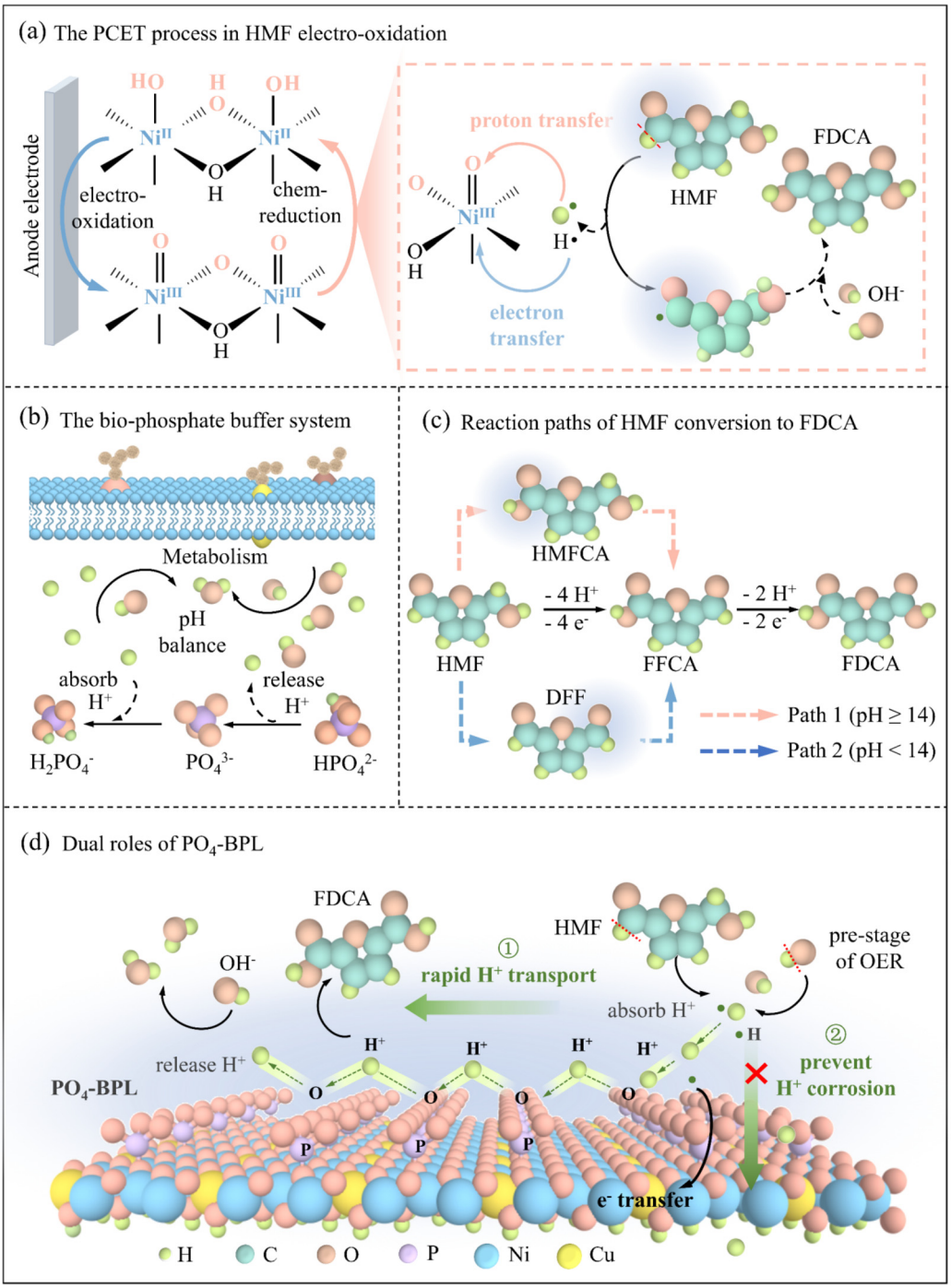

Scheme 1 (a) Schematic of the proton-coupled electron transfer (PCET) process with sluggish H transport during 5-HMF electro-oxidation. (b) Principles of the intracellular phosphate buffer system in biological cells. (c) Reaction pathways of FDCA formation. (d) Dual roles of the biomimetic phosphate-built protective layer (PO_4-BPL): creating rapid proton channels to enhance PCET and protecting the catalyst from proton-induced corrosion. HMF: 5-hydroxymethylfurfural, HMFCA: 5-hydroxymethyl-2-furancarboxylic acid, FFCA: 5-formyl-2-furancarboxylic acid, DFF: 2,5-diformylfuran, FDCA: 2,5-furan dicarboxylic acid.

2. Methods and materials

2.1 Chemicals

All the reagents mentioned above were not further treated. Potassium hydroxide (KOH, 90%), nickel nitrate hexahydrate ($Ni(NO_3)_2{\cdot}6H_2O$, 98%), copper nitrate trihydrate ($Cu(NO_3)_2{\cdot}3H_2O$, 98%), trisodium citrate (≥98%), disodium hydrogen phosphate (Na_2HPO_4, 99%), 5-hydroxymethyl-furfural (HMF, 99%), 2,5-diformylfuran (DFF, ≥98%), 5-hydroxymethyl-2-furancarboxylic acid (HMFCA, 98%), 5-formyl-2-fur-

Published on 21 November 2025. Downloaded on 5/17/2026 11:33:50 AM.

ancarboxylic acid (FFCA, ≥98%) and 2,5-furandicarboxylic acid (FDCA, 98%) were obtained from Aladdin Chemistry Co., Ltd. Nickel nitrate hexahydrate ($NiCl_2{\cdot}6H_2O$, 99%), methanol (for HPLC, ≥99.9%) and ethanol (≥99.5%) were purchased from Sinopharm Chemical Reagent Co., Ltd. Deionized water was used to prepared the aqueous solutions in all the experiments.

2.2 Preparation of PO_4-BPL/CuNiO

Substrate pretreatment: commercial Ni foam (NF, thickness 1.0 mm, porosity ~95%) was cut into 1.0 cm × 1.0 cm pieces (geometric area 1.0 cm^2). Each piece was ultrasonicated sequentially in acetone, 0.5 M HCl, ethanol, and 18.2 MΩ cm water for 10 min each (total 40 min), rinsed thoroughly with water, and dried in N_2 at 60 °C.

Co-electrodeposition of CuNiO base: a three-electrode cell (glass beaker, 30 mL electrolyte, 25 ± 0.5 °C) was used with NF as working electrode, Pt sheet (1 cm × 1 cm) as counter, and Ag/AgCl (3 M KCl, +0.210 V *vs.* SHE) as reference. The electrolyte contained 60 mM $Cu(NO_3)_2{\cdot}6H_2O$, 40 mM $NiCl_2{\cdot}6H_2O$, and 20 mM sodium citrate in water. Deposition was carried out galvanostatically at −50 mA cm^{-2} (−50 mA for 1 cm^2) for 10 min (controlled by an electrochemical workstation, CHI660E). After deposition the electrode was rinsed (3 × 10 mL water) and vacuum-dried at 60 °C, 6 h. The as-prepared composite is denoted CuNiO.

Hydrothermal phosphatization to form PO_4-BPL: a solution of 50 mM Na_2HPO_4 and 20 mM $Ni(NO_3)_2{\cdot}6H_2O$ (total volume 30 mL) was prepared and ultrasonicated for 30 min. A single CuNiO-coated NF (1 cm^2) was immersed, the mixture transferred to a Teflon-lined autoclave (50 mL, fill ≤ 60%), and held at 80 °C for 12 h (natural cooling to room temperature). The electrode was rinsed with water (3 × 10 mL) and vacuum-dried (60 °C, 6 h) to obtain PO_4-BPL/CuNiO.

PO_4-BPL/NiO was prepared identically but omitting $Cu(NO_3)_2{\cdot}6H_2O$ during electrodeposition but subjected to the same hydrothermal phosphatization.

2.3 Structural characterizations

XRD. Rigaku MiniFlex-600 (Cu Kα, λ = 1.5406 Å), 40 kV per 15 mA, 2θ = 10–80°, step 0.02°, 1° min^{-1}. Si 2θ was used for instrument alignment; SEM/TEM/EDS: SEM: ZEISS GeminiSEM 360 at 3–5 kV. TEM/EDS: JEOL JEM-2100F at 200 kV; XPS. Thermo Scientific K-Alpha (Al Kα, $h\nu$ = 1486.6 eV), charge neutralizer on. Binding energies were calibrated to C 1s = 284.8 eV; FT-IR. Nicolet iS5, ATR mode, 4000–500 cm^{-1}, 4 cm^{-1} resolution, 64 scans.

***In situ* Raman.** Horiba XploRA PLUS, 785 nm, 50× (NA = 0.5) long-working-distance objective. Acquisition 20 s per spectrum, 3 accumulations. Silicon at 520.7 cm^{-1} used for wavenumber calibration (±0.5 cm^{-1}). The Raman cell used a three-electrode configuration (working: as-prepared electrode; reference: Ag/AgCl; counter: Pt wire) in 1 M KOH with/without 50 mM HMF, potential-step protocol 1.10–1.7 V *vs.* RHE (step 50 mV, hold 60 s).

2.4 Electrochemical measurements

The electrochemical properties were tested by a CHI660E workstation, which utilizes a standard three-electrode system consisting of a prepared electrode (1 × 1 cm^2) as the working electrode, and Pt and Hg/HgO as the counter electrode and reference electrode, respectively. All tests were performed in an H-cell with FAA-3-50 membrane as a septum. Linear scanning voltammetry (LSV) was performed at a scan rate of 50 mV s^{-1} with 85% *iR* correction. All potentials were calibrated to a reversible hydrogen electrode (RHE) reference scale by applying the following eqn (1):

$$E_{RHE} = E_{measured} + E_{Hg/HgO} + 0.0591 \times pH \quad (1)$$

The electrochemically active surface area (ECSA) was derived from the specific capacitance (C_{dl}) of the bilayer. Cyclic voltammetry (CV) measurements were carried out in the non-Faraday potential range at different scan rates from 10 to 100 mV s^{-1} to obtain C_{dl}.

Electrochemical EIS measurements: use AC impedance way to test, in a frequency range from 100 kHz to 0.1 Hz, with an AC amplitude of 5 mV. Measurements were carried in a standard three-electrode configuration, the obtained spectra were fitted using ZView software with an appropriate equivalent circuit model.

The distribution of relaxation times (DRT) plot was obtained using a MATLAB tool developed by Ciucci *et al.*,[36,37] employing 0.01 regularization factor and Gaussian basis functions.

2.5 HPLC analysis of products

HMF and its oxidation products were analyzed by high performance liquid chromatography (HPLC, LC5090 system, UV-visible detector) equipped with a 4.6 mm × 250 mm Shim-pack GWS 5 μm C-18 column. The column temperature was 35 °C, and the mobile phase was methanol : 5 mM ammonium formate solution (3 : 7) at a flow rate of 0.6 mL min^{-1}. The UV detection wavelength was 265 nm. The HMF conversion, FDCA selectivity, and faradaic efficiency of FDCA were calculated according to the following formula:

$$\text{HMF conversion}\,(\%) = n(\text{consumed HMF})/n(\text{initial HMF}) \times 100\% \quad (2)$$

$$\text{FDCA selectivity}\,(\%) = n(\text{FDCA formed})/n(\text{consumed HMF}) \times 100\% \quad (3)$$

$$\text{Faradaic efficiency}\,(\%) = 6 \times n(\text{FDCA formed}) \times F/\text{total charge passed} \times 100\%. \quad (4)$$

2.6 Computational details

All DFT calculations in this work were conducted using the Vienna *ab initio* simulation package software (VASP). All electronic structures are calculated using the generalized gradient approximation (GGA), unfolding the perdew – burke erzerhof

 This journal is © The Royal Society of Chemistry 2026

Published on 21 November 2025. Downloaded on 5/17/2026 11:33:50 AM.

(PBE) in a plane wave substrate with the cutoff energy set to 450 eV. A 1 × 1 × 1 Monkhorst–Pack *k*-point grid sampling was used for Brillouin zone integration to optimize all surface structures. Equilibrium was reached when the force on the relaxing atoms was less than 0.03 eV A^{-1} and the energy of the self-consistent iteration was less than 10^5 eV. The CuNiOOH body was constructed by replacing a Ni atom with a Cu atom, which consists of stoichiometric NiOOH. A 20 Å vacuum layer was used to eliminate interactions between neighboring plates. All transition states (TS) were rigorously validated by harmonic frequency analyses at the same level of theory, confirming that each optimized geometry exhibits exactly one imaginary vibrational frequency corresponding to the reaction coordinate.

3. Results and discussion

3.1 Characterization of the PO_4-BPL/CuNiO catalyst

The PO_4-BPL/CuNiO catalyst was synthesized through a sequential electrochemical deposition and hydrothermal phosphidation protocol as detailed in SI. The surface morphology of CuNiO (Fig. S1) and PO_4-BPL/CuNiO (Fig. 1a) indicates that minute protrusions formed on the electrocatalyst surface after phosphidation. Nevertheless, the overall structure retained its integrity, and the catalyst's original morphology was preserved without significant framework distortion. The EDS results (Fig. S2 and S3) confirmed that the elements of P, O, Cu and Ni were homogeneously distributed on the phosphidated catalyst surface. This spatial uniformity demonstrates effective metal dispersion and conformal phosphate grafting throughout the nickel foam substrate. The SEM-EDS cross-sectional imaging (Fig. S4) shows a uniform catalyst film ~1 μm thick on the Ni foam. Line scans from top to bottom reveal uniform Cu and Ni signals across the entire thickness, while P is present throughout the layer. These data confirm that hydrothermal phosphatization produces a PO_4-BPL that coats the full catalyst layer, not just the surface. Further XRD analysis demonstrates a stronger NiO peak signal after phosphidation, suggesting enhanced crystallinity during phosphate incorporation (Fig. S5). Addition, N_2 physisorption at 77 K on PO_4-BPL/CuNiO and CuNiO (Fig. S6) shows that the overall pore distribution remains unchanged, yet the number of pores below 10 nm increases after phosphatization. This confirms the formation of additional microstructures, consistent with SEM observations.

Atomic-resolution structural analysis of PO_4-BPL/CuNiO was conducted *via* high-resolution TEM on ultrasonically exfoliated fragments (Fig. 1b), revealing an amorphous core surrounded by surface crystalline domains with distinct lattice fringes. Selected-area EDS (Fig. S7) identified the crystalline regions as NiO, with PO_4 and Cu enriched on the surface. Lattice parameter analysis aligned with XRD data confirmed the predominant exposure of NiO (101) planes. TEM-EDS mapping (Fig. 1c) demonstrated uniform distribution of Cu and PO_4 within the catalyst matrix. Comparative FTIR analysis (Fig. 1d) revealed intensified P–O vibrational modes (900–1100 cm^{-1}), confirming successful PO_4 grafting post-phosphidation. XPS analysis elucidated the chemical states of Ni and Cu. The Ni 2p spectrum (Fig. 1e) exhibited dual oxidation states: Ni^{2+} (856.38 eV, $2p_{3/2}$; 874.28 eV, $2p_{1/2}$) and Ni^{3+} (858.18 eV, $2p_{3/2}$; 876.58 eV, $2p_{1/2}$), supported by satellite peaks at 862.98 eV and 880.95 eV.[38,39] The Cu 2p spectrum featured Cu^0 (932.58 eV, $2p_{3/2}$; 952.18 eV, $2p_{1/2}$) and Cu^{2+} (935.48 eV, $2p_{3/2}$; 954.78 eV, $2p_{1/2}$), with satellite peaks at 943.28 eV and 962.68 eV.[35,40,41] The P 2p spectrum (Fig. S8) exclusively dis-

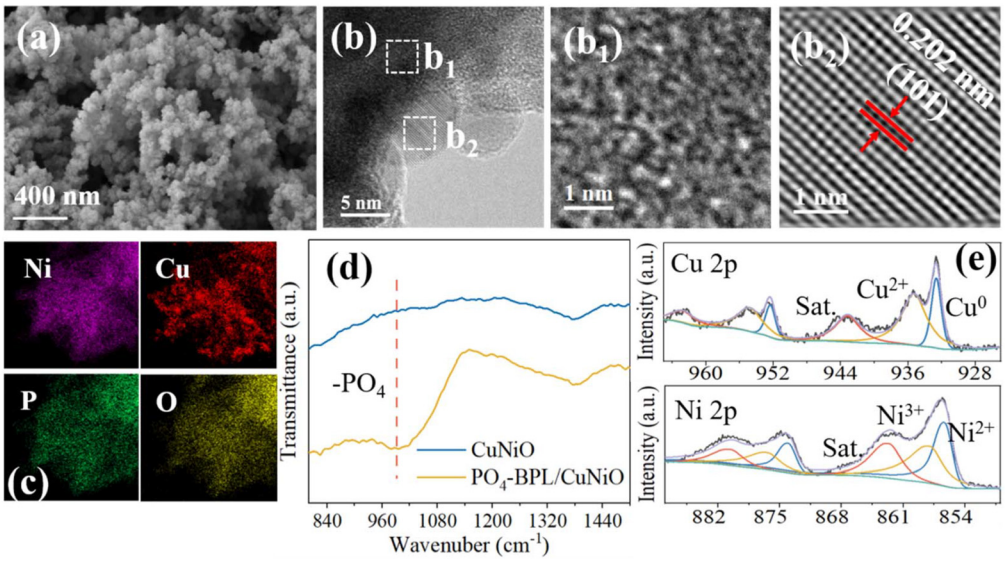

Fig. 1 (a) SEM image of PO_4-BPL/CuNiO, (b) TEM results of PO_4-BPL/CuNiO, (b1) TEM results of the amorphous part, (b2) TEM results of the NiO lattice part, (c) TEM-EDS results of PO_4-BPL/CuNiO, (d) FTIR results of PO_4-BPL/CuNiO, (e) XPS peak fitting results of Cu and Ni elements in PO_4-BPL/CuNiO.

Published on 21 November 2025. Downloaded on 5/17/2026 11:33:50 AM.

played a PO_4^{3-} peak at 133.4 eV, and the characteristic peak of elemental P did not appear.[42] A comparative analysis of the O 1s XPS spectra before and after hydrothermal phosphorylation reveals the presence of P–O–M bonds on the catalyst surface (Fig. S9). After phosphorylation, a distinct P–O–M peak emerges at approximately 533 eV, while the oxygen vacancy peak at 531.5 eV remains largely unchanged.[43,44] These results confirm the formation of stable chemical bonds between phosphate groups and the catalyst precursor during hydrothermal phosphorylation. XPS analysis was performed on the CuNiO base (without PO_4-BPL), as shown in Fig. S10. Comparison with the valence states of the hydrothermally phosphorylated catalyst (Fig. 1(e)) indicates no change in the oxidation states of metallic Ni and Cu. These results collectively confirm the successful synthesis of the PO_4-BPL/CuNiO catalyst.

3.2 Electrochemical performance of HMF oxidation

The electrochemical performance was tested in a standard three-electrode configuration. In this setup, PO_4-BPL/CuNiO served as the working electrode, 1 M KOH functioned as the electrolyte, a Pt sheet was employed as the counter electrode, and Hg/HgO acted as the reference electrode. All potentials were calibrated to the reversible hydrogen electrode (RHE) scale. Fig. 2a depicts the linear sweep voltammetry (LSV) curves of different electrodes in a solution containing 50 mM HMF. The results indicate that PO_4-BPL/CuNiO exhibits the highest current density for HMF conversion. Notably, when the potential is only 1.44 V, the current density can reach 500 mA cm^{-2}, and when the potential increases to 1.51 V, the current density can reach an impressive 700 mA cm^{-2}. A comparison of the electrocatalytic performance with and without the PO_4-BPL reveals that the presence of PO_4-BPL significantly enhances the conversion efficiency of HMF. However, it has a negligible effect on OER. This suggests that PO_4-BPL can significantly promote the transfer of electrons/protons during HMF conversion. Fig. 2b presents the LSV results of PO_4-BPL/CuNiO under varying HMF concentrations. The results demonstrate that the current density increases significantly with higher HMF concentrations. Notably, at an HMF concentration of 100 mM, a current density of 700 mA cm^{-2} is achieved at a potential of just 1.39 V. This indicates that PO_4-BPL/CuNiO possesses substantial oxidizing ability for HMF, with the current density positively correlating with the HMF concentration. As shown in Fig. 2c, the plot reveals the potential required for different catalysts to attain specific current densities. The data demonstrate that PO_4-BPL/CuNiO consistently requires the lowest potential across all current densities examined. This finding underscores the superior performance of PO_4-BPL/CuNiO in the electrocatalytic conversion of HMF.

To gain a deeper understanding of the intrinsic activity of CuNiO and PO_4-BPL/CuNiO, the differences in their electrochemical active surface areas were further investigated. The electrochemical surface area (ECSA) was determined through double-layer capacitance (C_{dl}) measurements derived from cyclic voltammetry (CV) scans at varying rates (10–100 mV s^{-1}) in the non-faradaic region (Fig. S11). As shown in Fig. 2d, the C_{dl} values of CuNiO and PO_4-BPL/CuNiO were 3.07 mF cm^{-2} and 4.27 mF cm^{-2}, respectively. Combined with the SEM results, there were no significant changes in the surface structures of CuNiO and PO_4-BPL/CuNiO, indicating that phosphate functionalization enhances the density of electrochemically active sites. The kinetics during the reaction were examined using Tafel slopes. As shown in Fig. 2e, the Tafel slopes for CuNiO and PO_4-BPL/CuNiO in the OER and HMF electro-oxidation processes were calculated. During the OER process, there was little difference in the slopes of CuNiO and PO_4-BPL/CuNiO. However, a significant difference was observed during HMF electro-oxidation, indicating that PO_4 accelerated the HMF electro-oxidation reaction. This renders the interfacial electron transfer between HMF molecules and the catalyst more efficient, thereby resulting in a lower adsorption potential of HMF on the electrode. Furthermore, Nyquist plots were used to investigate the electron transfer and reaction kinetics of CuNiO and PO_4-BPL/CuNiO under alkaline conditions with HMF. Fig. S12 is the equivalent fitting circuit diagram, and Table S1 exhibited the values of equivalent fitting circuit diagram. As shown in Fig. 2f, smaller charge transfer resistance compared to the PO_4-BPL-free surface. This indicates that the resistance to be overcome in the HMF electro-oxidation reaction was greater for CuNiO. This finding suggests that the PO_4-BPL at the PO_4-BPL/CuNiO interface facilitates electron transfer, resulting in faster reaction kinetics.

The electrocatalytic conversion experiment of HMF was conducted in an H-type reactor. The anode electrolyte was a mixed solution of 1 M KOH and 50 mM HMF, while the cathode electrolyte was 1 M KOH. Two potential oxidation pathways exist for the conversion of HMF to FDCA (Scheme 1c). In Path I, the aldehyde group of HMF is first oxidized to a carboxyl group, forming 5-hydroxymethyl-2-furan carboxylic acid (HMFCA) as an intermediate. Subsequently, the hydroxymethyl group of HMFCA is further oxidized to an aldehyde group, yielding another intermediate, 2-formyl-5-furan carboxylic acid (FFCA). Finally, the aldehyde group of FFCA is oxidized to a carboxyl group, resulting in FDCA.[45] In Path II, the hydroxymethyl group of HMF is first oxidized to form 2,5-diformylfuran (DFF), which is then further oxidized to convert the surface aldehyde groups to carboxyl groups, producing FFCA, and ultimately oxidized to FDCA.[46,47] Since each HMF molecule requires six electrons to be converted into FDCA, it is calculated that 57.8 C of charge is needed to completely convert 10 mL of 10 mM HMF into FDCA in the experiment. Fig. 3a illustrates that as the charge transferred increases, the HMF concentration in the system decreases rapidly, while the FDCA concentration rises correspondingly. Once the charge reaches 57.8 C, HMF and other intermediates are nearly undetectable, indicating nearly complete conversion to FDCA. During the conversion, the intermediate DFF is barely detectable, and HMFCA remains at a low concentration, suggesting the conversion proceeds mainly through the HMF-HMFCA-FFCA-FDCA pathway. The rapid intermediate conversion results in no significant accumulation of these products, achieving 100% FDCA conversion.

 This journal is © The Royal Society of Chemistry 2026

Published on 21 November 2025. Downloaded on 5/17/2026 11:33:50 AM.

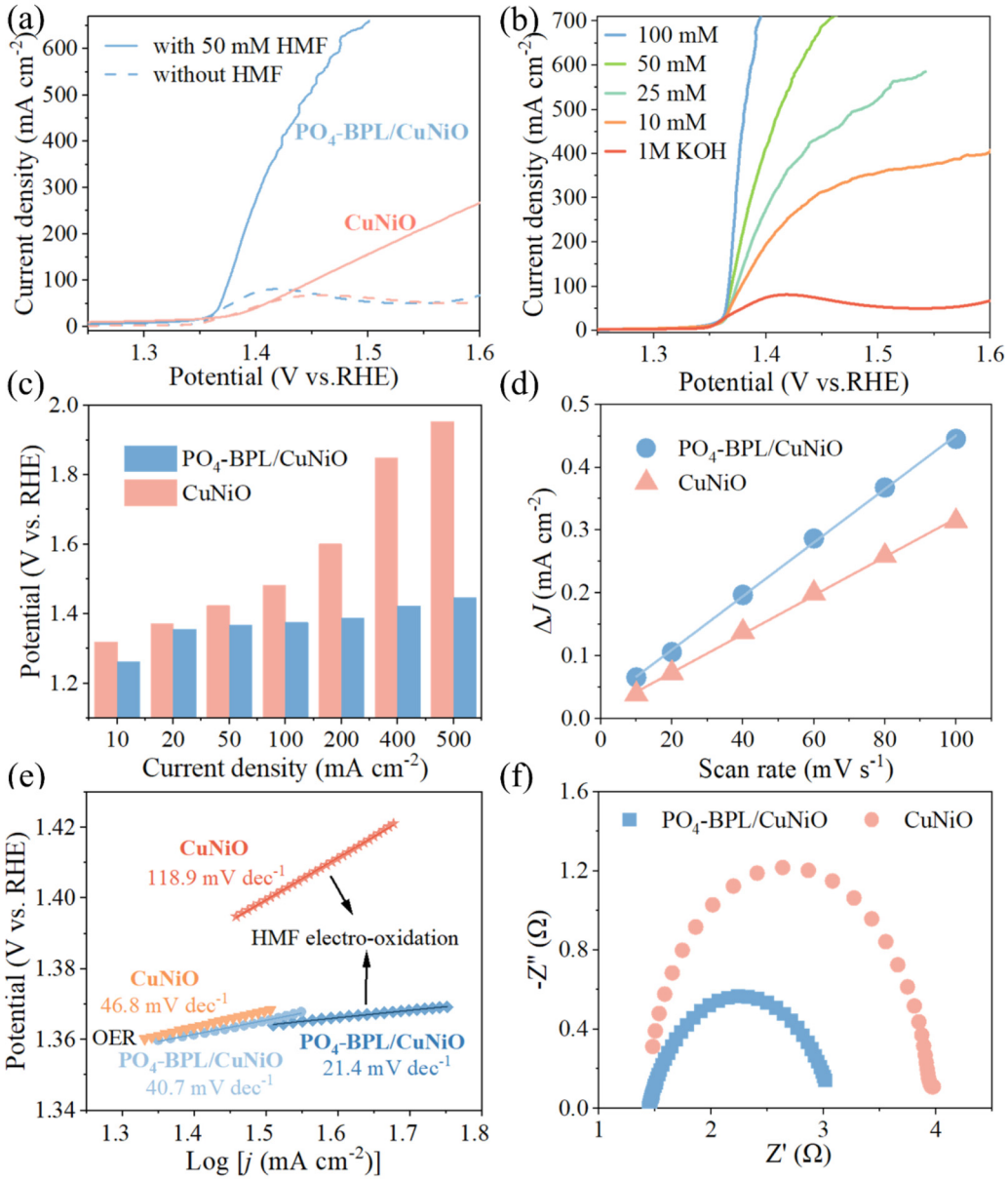

Fig. 2 (a) LSV curves of PO_4-BPL/CuNiO, CuNiO in 1 M KOH solution with/without 50 mM HMF. (b) LSV curves of PO_4-BPL/CuNiO in 1 M KOH solution with different concentrations of HMF. (c) The potential required for PO_4-BPL/CuNiO, CuNiO to reach different current densities. (d) The double-layer capacitance of PO_4-BPL/CuNiO, CuNiO. (e) Tafel curves of PO_4-BPL/CuNiO and CuNiO in OER and HMF electro-oxidation reactions. (f) Nyquist plots of PO_4-BPL/CuNiO, CuNiO in 1 M KOH with 50 mM HMF.

HMF conversion experiments were performed at different potentials, with the results shown in Fig. 3b. The results show that the Faraday efficiency of FDCA increases with increasing potential, and the Faraday efficiency can be more than 95% starting from 1.4 V. And the corresponding current density increases significantly, further confirming the strong conversion to HMF. This highlights the exceptional efficiency and selectivity of PO_4-BPL/CuNiO in the conversion of HMF to FDCA. However, at 1.6 V, the faradaic efficiency of FDCA declines, likely due to competitive OER reactions at the anode caused by the high potential. Based on these results, within the potential window of 1.4–1.55 V, the faradaic efficiency of FDCA for PO_4-BPL/CuNiO remains above 95%, indicating a relatively broad electrochemical reaction window. At 1.55 V, FDCA selectivity and HMF conversion capacity were maximized and the rate of current density increase was balanced, thus, 1.55 V was the optimal conversion potential. Fig. S13 shows the results of *i–t* curve at 1.55 V. The current gradually decreased with increasing time and substrate consumption. Fig. 3c shows that HMF is gradually converted to FDCA with increasing charge transfer, and the concentration of intermediates remains stable. This indicates that the PO_4-BPL/

Published on 21 November 2025. Downloaded on 5/17/2026 11:33:50 AM.

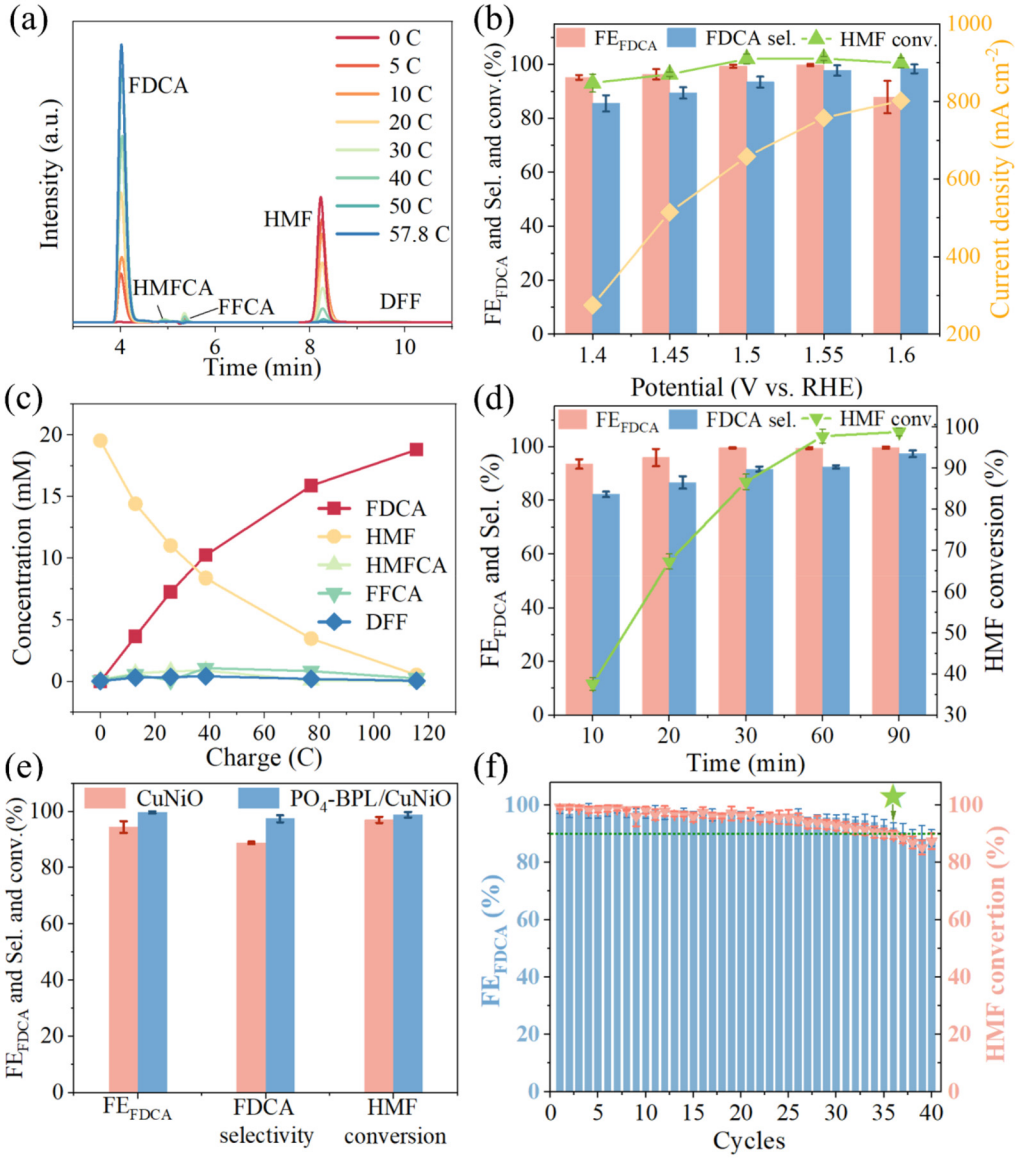

Fig. 3 (a) HPLC chromatogram as charge accumulates. (b) Faradaic efficiency, selectivity of FDCA, conversion rate of HMF and current density for PO_4-BPL/CuNiO at different potentials at 50 mM HMF. (c) The concentration of HMF and its oxidation products during HMF electro-oxidation at 1.55 V. (d) Faradaic efficiency, selectivity of FDCA, and conversion rate of HMF for PO_4-BPL/CuNiO at different times at 1.55 V and 50 mM HMF. (e) Compare the faradaic efficiency of FDCA, FDCA selectivity, and HMF conversion rate for different catalysts at 1.55 V under a 10 mM HMF concentration. (f) Cyclic performance of PO_4-BPL/CuNiO under 10 mL 10 mM HMF conditions at 1.55 V.

CuNiO catalyst can transfer the intermediate products rapidly. Fig. 3d shows the conversion of HMF over a long period of time in H type reactor, and the FDCA selectivity and Faraday efficiency and HMF conversion gradually increased with increasing time. Fig. S14 presents photographs of the HMF solution during electro-oxidation. The 50 mM HMF solution is yellow before electrolysis. As the reaction proceeds, the color fades to colorless, demonstrating the high degradation activity of PO_4-BPL/CuNiO. As shown in Fig. 3e, PO_4-BPL/CuNiO was higher than CuNiO in terms of Faraday efficiency, FDCA selectivity and HMF conversion, which further verified the great potential of PO_4-BPL in the electrocatalytic conversion of HMF.

The cyclic stability of the PO_4-BPL/CuNiO electrode for HMF electro-oxidation was investigated by applying a constant potential of 1.55 V in 10 mL of electrolyte containing 1 M KOH and 10 mM HMF. After each run, the total charge reached 57.8 C, and then 10 mL of fresh electrolyte was replaced. The faradaic efficiency of FDCA and the conversion rate of HMF remained above 90% for 36 consecutive cycles (Fig. 3f). In contrast, the cyclic stability of the CuNiO electrode (Fig. S15) exhibited rapid performance decay (FE_{FDCA}<90% after 5 cycles). The stability of the PO_4-BPL/CuNiO electrode was 7 times that of CuNiO, indicating that PO_4-BPL can significantly enhance the cyclic stability of the catalyst. The PO_4-BPL/CuNiO

This journal is © The Royal Society of Chemistry 2026

Published on 21 November 2025. Downloaded on 5/17/2026 11:33:50 AM.

electrode after the reaction was characterized by SEM and XPS. According to the SEM results (Fig. S16 and S17), the surface structure of the catalyst remained stable after the cyclic reaction, with no obvious collapse, and Cu, Ni, and P were still evenly distributed. XPS results indicated an increased proportion of Ni^{3+}, high-valent Cu, unchanged P valence, and a slight decrease in P content post-reaction. These changes are attributed to the anodic oxidation reaction, where the catalyst participates through high-valent states, leading to an overall potential increase. These findings demonstrate that PO_4-BPL/CuNiO maintains excellent activity and structural stability during HMF conversion. The CuNiO without PO_4-BPL after the cyclic reaction was characterized using SEM-EDS and XPS, with the results shown in Fig. S18 and Table S2. Comparing the SEM results with and without PO_4-BPL protection, it can be observed that, although the basic structure of the catalyst without PO_4-BPL protection remains largely intact, significant cracks have formed in the catalyst layer, and there are signs of catalyst peeling. The catalyst without PO_4-BPL protection resulting in a significant reduction in the active component content and catalyst deactivation. The significant decline in FE and HMF conversion after 40 cycles is attributed to gradual catalyst degradation, though the achieved stability already exceeds most reported systems (Table S3). Post-reaction characterization (Fig. S3 and S17) shows decreased Cu and Ni atomic ratios and reduced surface PO_4 content, indicating deactivation primarily originates from active-site loss and catalyst detachment. Repeated cycling weakens the PO_4-BPL, causing PO_4 leaching and NiOOH exposure, while prolonged operation under local acidity and potential fluctuations accelerates degradation. Consequently, activity drops, HMF conversion is limited, and intermediate accumulation lowers FE.

Owing to the excellent recyclability of the PO_4-BPL catalyst in an H-type cell, we designed and assembled a continuous-flow electrolyzer (Fig. S19 and Fig. 4a). This device reduces concentration polarization and improves mass transfer, enabling a high current density. The cell contains an anion-exchange membrane with an active area of 2 cm × 2 cm. The anode is coated with the PO_4-BPL catalyst, and the cathode is nickel foam. At 10 mM HMF, the system continuously converts HMF to FDCA. A peristaltic pump circulates the anolyte and catholyte, supplying reactants to and removing products from the electrode surfaces. The LSV curve of PO_4-BPL shows that, at 200 mA cm^{-2}, the cell voltage for HER coupled with HMF oxidation (HER/HMFOR) is 320 mV lower than that for HER coupled with oxygen evolution (HER/OER) when the catholyte is 1 M KOH and the anolyte is 1 M KOH plus 50 mM HMF (Fig. 4b) (all voltages in this part are uncorrected, the results of EIS of the flow electrolyzer are showing in Fig. S20). This result confirms that PO_4-BPL is highly active for HMF electro-oxidation at industrially relevant current densities. During continuous current electrolysis at 200 mA cm^{-2}, no gas bubbles appeared on the anode, indicating that the competitive oxygen evolution reaction is suppressed in the HMFOR/HER continuous-flow electrolyzer. More importantly, PO_4-BPL retains its activity over 70 h, whereas the unprotected catalyst loses activity after only 6 h, as shown by a sharp increase in cell voltage (Fig. 4c). The comparison demonstrates that PO_4-BPL

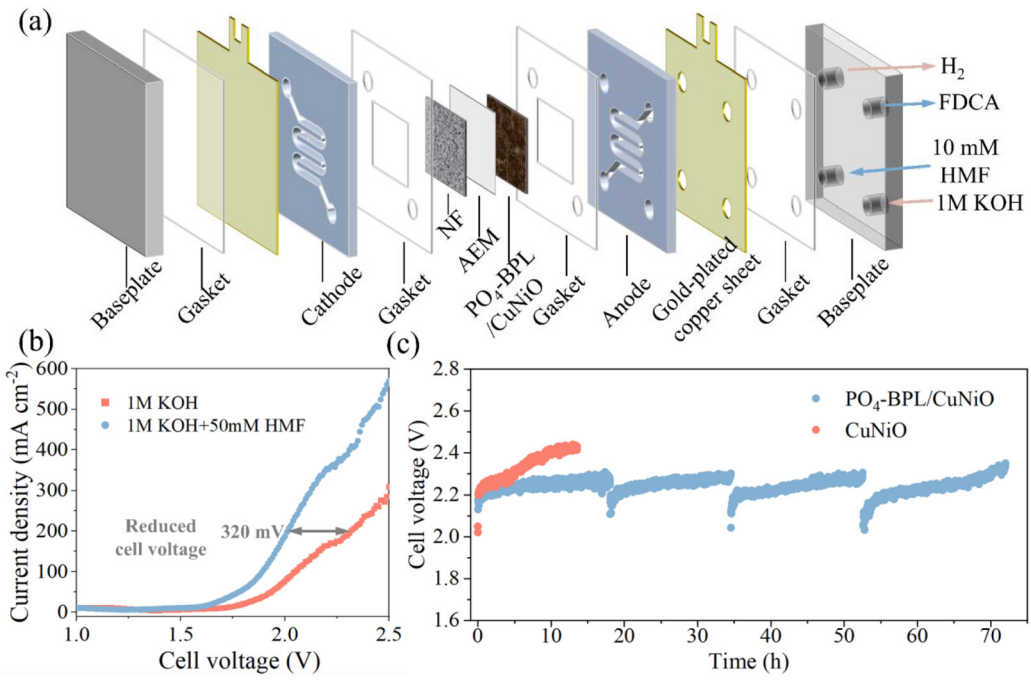

Fig. 4 (a) Internal structure diagram of the continuous-flow electrolyzer, (b) LSV curves of PO_4-BPL/CuNiO in 1 M KOH with or without 50 mM HMF in a continuous-flow electrolyzer (with 85% *iR* compensation), (c) cell voltage of PO_4-BPL/CuNiO and CuNiO during continuous operation at 200 mA cm^{-2} for over 70 h.

Published on 21 November 2025. Downloaded on 5/17/2026 11:33:50 AM.

markedly improves catalyst durability and supports the proposed protective role of the PO_4 layer.

Compared with previously reported catalysts, PO_4-BPL catalysis delivers superior performance in maximum current density, HMF conversion, FDCA selectivity, faradaic efficiency, and cycling stability (Table S3). These results confirm its operational stability during continuous HMF conversion and demonstrate its strong potential for industrial-scale HMF-to-FDCA transformation.

3.3 *In situ* characterization for HMF oxidation

To further clarify the reaction mechanism of the PO_4-BPL/CuNiO catalyst throughout the HMF electro-oxidation reaction process, *in situ* Raman characterization was performed to observe surface reconstruction and identify active sites involved in the reaction, with the results presented in Fig. 5a and b. This characterization compared the surface states of the PO_4-BPL/CuNiO catalyst in the presence and absence of HMF. The peak observed at 335 cm^{-1} is attributed to CuO,[48,49] while the peaks at 474 cm^{-1} and 557 cm^{-1} correspond to Ni^{3+}–O.[35,41] In 1 M KOH electrolyte, the OER-related changes were first examined. When the potential exceeds 1.3 V, the characteristic Ni^{3+}–O peaks at 474 cm^{-1} and 557 cm^{-1} become prominent (Ni^{II}–O-e^- → Ni^{III}–OOH), with their intensity increasing as the potential rises. In the HMF-containing electrolyte, once the applied potential exceeds 1.3 V, the Raman bands at 474 cm^{-1} and 557 cm^{-1}, assigned to Ni^{3+}, remain observable but with reduced intensity, implying rapid consumption of *in situ* generated Ni^{3+}OOH by HMF (Ni^{III}–OOH + HMF → products + Ni^{II}–O), and HMF was continuously transformed at the active

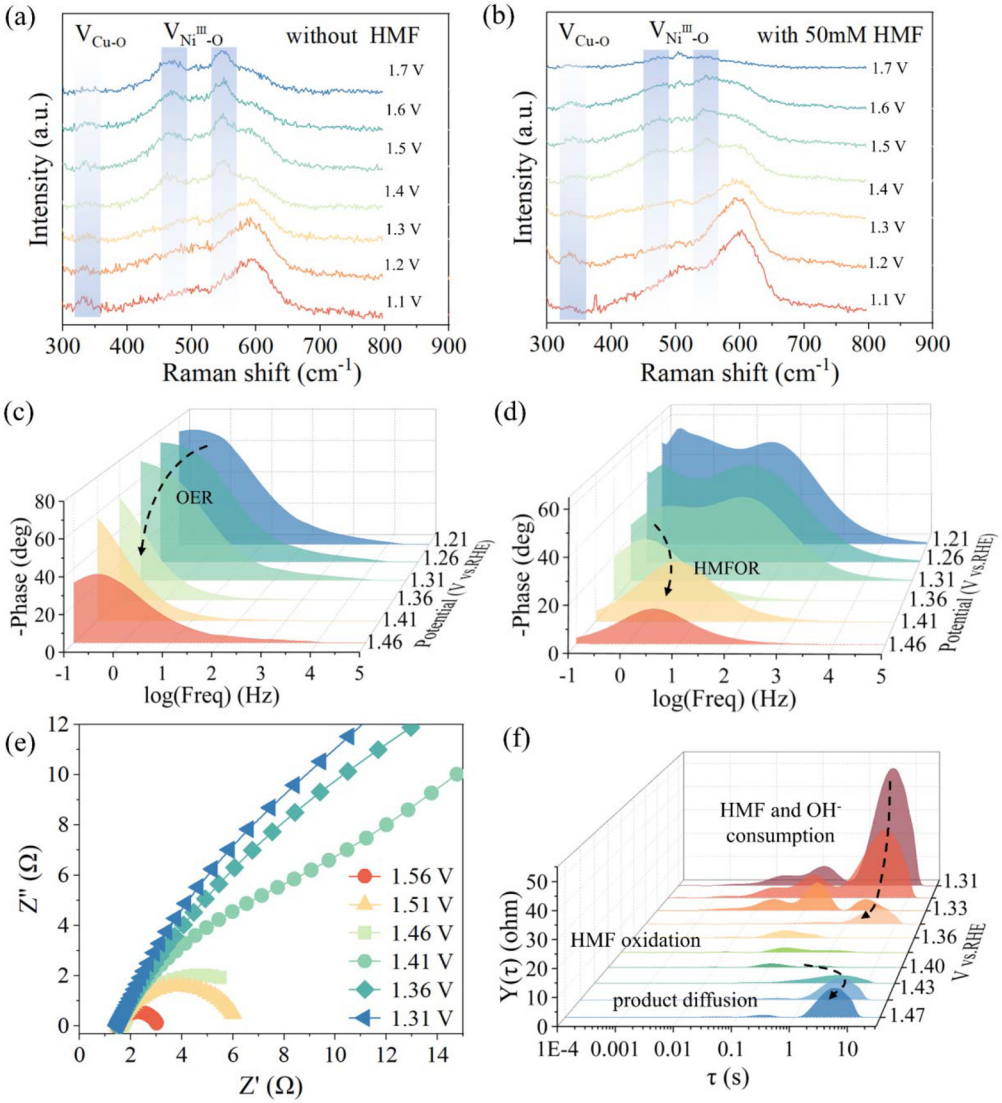

Fig. 5 *In situ* Raman spectra of PO_4-BPL/CuNiO electrodes during (a) OER (1.0 m KOH) and (b) HMFOR (1 M KOH with 50 mM HMF) under increasing potential from 1.1 to 1.5 V. Bode phase plots of the *in situ* electrochemical impedance spectra of PO_4-BPL/CuNiO (c) in the OER process, (d) in the HMFOR process. (e) Nyquist plots of PO_4-BPL/CuNiO at different potentials. (f) DRT fitting of PO_4-BPL/CuNiO in 50 mM HMF solution at different potentials.

This journal is © The Royal Society of Chemistry 2026

Published on 21 November 2025. Downloaded on 5/17/2026 11:33:50 AM.

sites as the potential increased.[50] Consequently, NiOOH emerges as the principal active species on the PO_4-BPL/CuNiO surface.

In the presence of PO_4-BPL, the CuO peak intensity remains largely unchanged during the reaction. In contrast, without PO_4-BPL, the CuO peak intensity increases with rising potential, further demonstrating the protective role of PO_4-BPL in maintaining catalyst structural stability. Meanwhile, we monitored the surface species evolution of the PO_4-BPL/CuNiO catalyst during electrocatalysis from 1.1 to 1.35 V *vs.* RHE using *in situ* Raman spectroscopy. The results further demonstrate that the PO_4-BPL facilitates proton transfer and stabilizes the catalyst structure (Fig. S21).

With the PO_4-BPL electrode, phosphate vibrations appear mainly in the ν_4 region (540–630 cm^{-1}) and the ν_1/ν_3 region (950–1050 cm^{-1}). Due to interference from organic vibrations and baseline drift, the ν_1/ν_3 modes were unresolved. We therefore focused on the more stable $\nu_4(PO_4)$ region. As shown in Fig. S21(a), the $\nu_4(PO_4)$ band intensity increases monotonically with potential from 0.10 to 0.35 V, accompanied by a slight shift. We attribute these spectral changes to potential-driven equilibria between PO_4^{3-} and HPO_4^{2-} and between P–O(H)···M and P–O–M bonding. This spectral evolution provides direct *in situ* evidence that the PO_4-BPL dynamically accepts protons (H^+) generated during HMF oxidation *via* conversion of phosphate species. These observations visually confirm the proton relay process, supporting the proposed role of the phosphate layer as a proton buffer that facilitates proton-coupled electron transfer.

In contrast, without the PO_4-BPL, a characteristic CuO peak emerges at 330–350 cm^{-1} and intensifies with increasing potential (Fig. S21(b)), indicating oxidation of the metallic Cu framework. In the presence of PO_4-BPL, the CuO signal does not increase noticeably, indicating suppressed or delayed Cu oxidation. Together, these findings show that the PO_4-BPL mitigates corrosive oxide formation, preserves the conductive framework, and enhances proton transport.

To further illustrate the changes on the electrode surface during the HMF electro-oxidation, bode plots and *operando* EIS were used to monitor the interfacial kinetics and electron transfer during the electrochemical reaction. Bode plots reveal the electrochemical processes of OER and HMF electro-oxidation. The high-frequency region (10^1–10^5 Hz) corresponds to the charge transfer within the electrode, while the low-frequency region (0.01–10 Hz) corresponds to the diffusion of reactants and generated oxidized substances on the electrode surface.[39,51] The *in situ* Bode plots of the PO_4-BPL/CuNiO electrode surface are shown in Fig. 5c and d. When comparing electrolyte conditions with and without HMF at a potential of 1.21–1.36 V, evident OH^- adsorption/diffusion on the electrode surface occurs in the OER system.[52] As the potential increases, the surface adsorption of OH^- gradually decreases, while the generated O_2 begins to diffuse. This results in significant O_2 diffusion resistance in the 10^1–10^3 Hz region. Under HMF electro-oxidation conditions at 1.21–1.36 V, besides reactant (HMF and OH^-) adsorption/diffusion on the electrode surface, a significant electron transfer peak of Ni^{2+} to Ni^{3+} in the mid-frequency region (10^1–10^3 Hz) is observed, which weakens with increasing potential. At 1.36 V, the product diffusion signal appears, and with further potential increase, product diffusion internal resistance accounts for a larger proportion of the total resistance, and the corresponding peak becomes more pronounced. In the HMF electro-oxidation system, signals for both HMF oxidation and simultaneous Ni^{3+} formation in the mid-frequency region are uniquely observed. This indicates that the PO_4-BPL/CuNiO electrode possesses a strong oxidation ability for HMF. The PO_4-BPL/CuNiO catalyst was further assessed with *operando* EIS in an electrolyte containing 50 mM HMF, and the resulting Nyquist plots at 1.30–1.55 V are shown in Fig. 5e. When the potential increased from 1.2 V to 1.35 V, the interfacial impedance (R_{ct}) rapidly decreased. The Nyquist plots showed an approximate straight line at low potentials of 1.30–1.40 V, indicating a high charge transfer resistance. When the applied potential exceeded 1.40 V, a distinct semicircle appeared, indicating a rapid electron transfer process on the electrode surface and the occurrence of HMF electro-oxidation, which was consistent with the results of the LSV curves. Meanwhile, by comparing the EIS in the electrolyte without the addition of HMF (Fig. S22), the Nyquist plots of the PO_4-BPL/CuNiO electrode showed an approximate vertical line in the range of 1.30–1.55 V, indicating a high charge transfer resistance for the OER reaction on the surface of the PO_4-BPL/CuNiO electrode.

To elucidate the kinetic processes and interfacial properties of the reactions on the surface of the PO_4-BPL/CuNiO electrode, Distribution of Relaxation Times fitting (DRT fitting) was performed on the impedance results (Fig. S23). The DRT fitting results indicate that multiple kinetic processes occurred on the electrode surface in OER and HMF electro-oxidation. Below 1.36 V, the impedance contribution from the adsorption of OH^- and HMF dominates. When the potential reaches ≥1.36 V, surface reconstruction initiates on the catalyst surface, forming NiOOH, consistent with *in situ* Raman spectroscopy results. In OER, oxygen evolution products begin diffusing outward from the electrode surface after 1.41 V. In HMF electro-oxidation, HMF continuously reacts with NiOOH, and the impedance contribution from electrode reconstruction remains stable. For more detailed impedance DRT fitting in the HMF electro-oxidation system, refer to Fig. 5f. As the potential increases, the adsorption resistance of HMF and OH^- on the electrode surface gradually decreases. With the occurrence of surface reconstruction, HMF reacts with the active sites, gradually consuming them, leading to a reduction in the surface reconstruction signal and the gradual release of products. A product diffusion peak appears in the range of τ = 1–10 s. This is consistent with the LSV results, indicating that after 1.36 V, HMF is converted, and the surface-reconstructed NiOOH serves as the main active site, possessing a rapid kinetic conversion capability for HMF. Furthermore, by comparing the DRT fitting results with and without BPL (Fig. S24), it is evident that the percentage contribution of adsorption impedance from OH^- and HMF significantly increases in the

Published on 21 November 2025. Downloaded on 5/17/2026 11:33:50 AM.

absence of PO_4-BPL. This indicates that the presence of the PO_4-BPL enhances the adsorption of OH^- and HMF on the electrode surface.

3.4 Mechanisms of the PO_4-built protective layer

Periodic electrochemical measurements were performed to verify the hydrogen transfer rate of the non-electrochemical step. First, the PO_4-BPL/CuNiO and CuNiO electrodes were maintained at a potential of 1.55 V for 150 s to generate a sufficient amount of NiOOH active sites on the catalyst surface. Subsequently, introducing HMF and switching the potential to the open-circuit potential allows the generated active sites to react with HMF. Once the current drops to 0 mA cm^{-2}, it signifies that the catalyst surface's accumulated active sites have fully reacted with HMF. This process reflects the reaction rate between the substrate and active sites, detectable *via* transient current monitoring. As shown in Fig. 6a, after the introduction of HMF, the current of PO_4-BPL/CuNiO dropped to 0 mA cm^{-2} more quickly than that of CuNiO within a shorter time, indicating that the H proton rapid transfer channel constructed by PO_4-BPL can indeed accelerate the PCET process in the electrocatalytic conversion of HMF. To

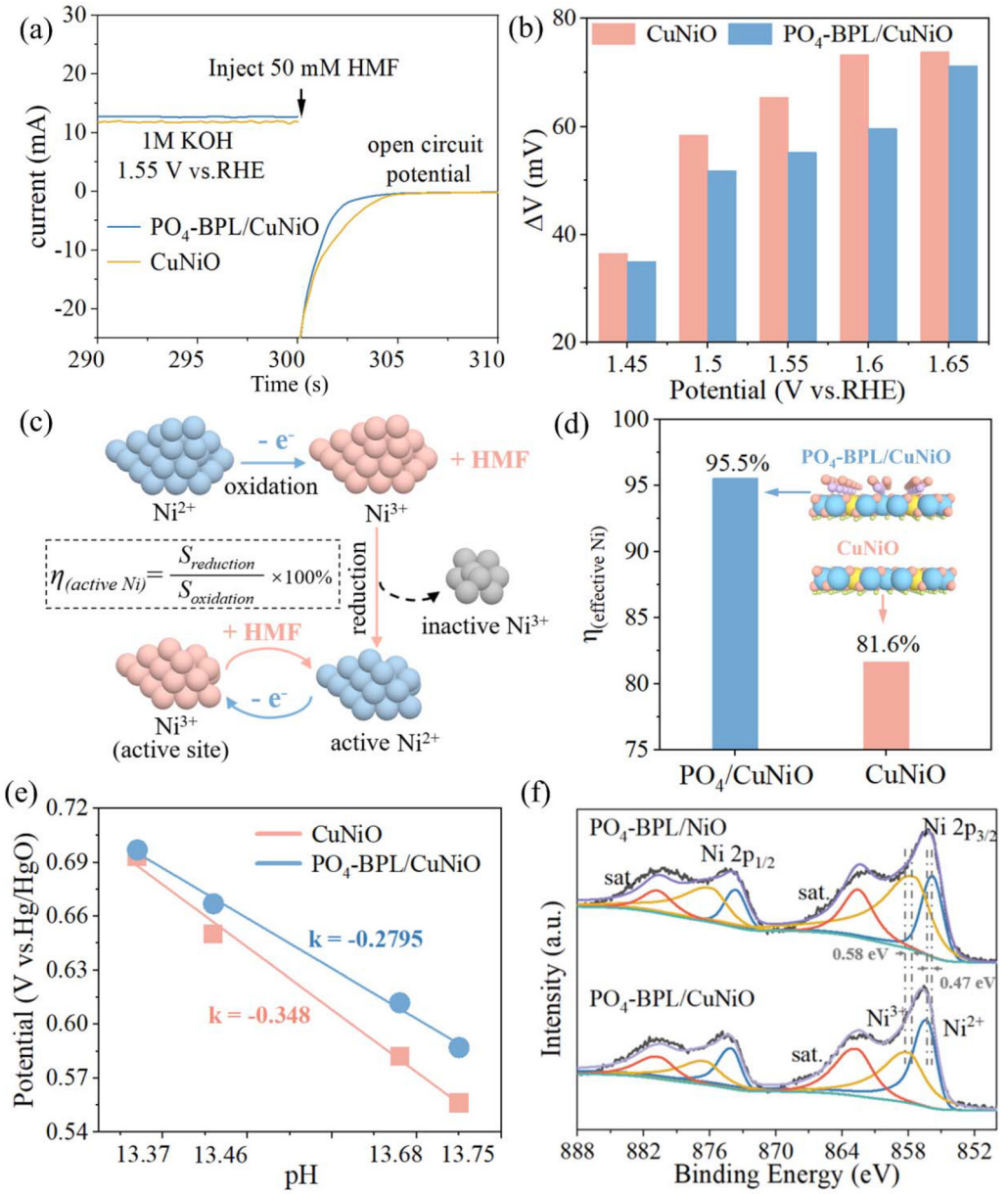

Fig. 6 (a) Periodic electrochemical measurements of PO_4-BPL/CuNiO and CuNiO. (b) Changes in open-circuit potential of PO_4-BPL/CuNiO and CuNiO after maintaining different potentials for 150 s. (c) Shifts in the Ni oxidation peak under different pH conditions of CuNiO and PO4-BPL/CuNiO. (d) Changes in valence state of Ni species during the reaction. (e)The ratio of the reduction peak area of Ni to the oxidation peak area in the CV curve PO_4-BPL/CuNiO and CuNiO. (f) XPS results of Ni with and without Cu doping.

 This journal is © The Royal Society of Chemistry 2026

Published on 21 November 2025. Downloaded on 5/17/2026 11:33:50 AM.

further illustrate the protective effect of PO_4-BPL on the catalyst surface microenvironment, the changes in the open-circuit potential of the electrode surface after the application of a long-term potential were compared. This comparison helps determine the characteristic changes in the catalyst surface double-layer, thereby indirectly reflecting the impact of OH^- protonation on the catalyst surface layer. The open-circuit potential changes after applying different potentials are shown in Fig. S25. As shown in Fig. 6b, compared with the CuNiO catalyst, the PO_4-BPL/CuNiO catalyst exhibited a smaller change in open-circuit potential after the application of a positive potential at the anode. For the CuNiO catalyst, as the potential increased, the active OH^- adsorbed in the double-layer on the electrode surface underwent oxygen evolution, generating H protons with strong destructive effects, which disrupted the surface double-layer structure. The protons could further contact and corrode the catalyst on the electrode surface. In contrast, in the PO_4-BPL/CuNiO catalyst, the surface PO_4-BPL not only enhanced the stability of the catalyst surface double-layer but also more effectively and rapidly scavenged the H protons produced by the oxygen evolution of adsorbed OH^- in the double layer, preventing them from damaging the double-layer structure and entering the interior of the catalyst. This resulted in a more stable double layer on the surface of the PO_4-BPL/CuNiO catalyst, hence the smaller change in open-circuit potential. Moreover, the larger the potential change for CuNiO, the slower the kinetics of the electrochemical reaction process. Therefore, the constructed PO_4-BPL increases the electrode reaction rate constant, lowers the reactants' activation energy on the electrode surface, and promotes rapid reaction progression.

In situ Raman spectra reveal that the surface-reconstructed NiOOH on the catalyst serves as the primary active site. However, not all Ni in the catalyst can be reconstructed *in situ* into active sites. In the anodic oxidation process, Ni^{2+} is first oxidized to Ni^{3+}, and with the deprotonation of HMF, the electrons and protons are given to the active site Ni^{3+}, which leads to the reduction of Ni^{3+} to Ni^{2+}, and in this process, the Ni^{3+} that cannot be reduced is the invalid site, and the Ni species that can be further reduced is the effective Ni^{2+}, and it is the effective Ni species that can serve as the active site in the HMF conversion (Fig. 6c). The percentage of effective Ni can be reflected by the ratio of the area of oxidation and reduction peaks of Ni in the catalyst's CV curve.[25] Fig. 6d and Fig. S26 show the CV curves of CuNiO and PO_4-BPL/CuNiO, with the proportion of the area of the Ni reduction peak to the oxidation peak calculated. By comparison, with the participation of the PO_4-PBL, the proportion of recyclable Ni in PO_4-BPL/CuNiO is higher, proving that more active Ni sites are present.

Additionally, the protective effect of the PO_4-BPL on the active site NiOOH under different pH conditions was investigated. As the potential increases, the catalyst surface undergoes reconstruction, with Ni^{2+} being oxidized to Ni^{III}–OOH, forming active sites. When the pH in the system increases, affected by the concentration of OH^-, the equilibrium constant of the redox reaction changes, enhancing the tendency for the reaction to proceed in the reverse direction, thus leading to a decrease in the metal oxidation peak potential. Therefore, by examining the shift in the Ni^{2+} oxidation peak under different pH values, the extent of the influence of OH^- in the system on the reaction of Ni^{2+} being oxidized to Ni^{III}–OOH can be determined. The CV curves of PO_4-BPL/CuNiO and CuNiO under different pH values are shown in Fig. 6e and Fig. S27. Compared to CuNiO, the change in the Ni^{2+} oxidation potential on the surface of PO_4-BPL/CuNiO is smaller and less pronounced. This indicates that the surface PO_4-BPL can reduce the impact of pH changes in the system on the reverse reaction of Ni^{2+} being oxidized to Ni^{III}–OOH, demonstrating the protective effect of the PO_4-BPL on the active site of NiOOH. Under 10 mM HMF (10 mL) conditions, the PO_4-BPL/CuNiO catalyst converts HMF to FDCA (57.8 C in theoretically) in a shorter time than the catalyst without PO_4-BPL (Fig. S28), demonstrating that PO_4^{3-} accelerates proton transfer and the overall reaction.

Comparing the presence and absence of Cu doping, the electrocatalytic performance of PO_4-BPL/NiO see Fig. S29, showed that the addition of Cu promotes the electrocatalytic conversion of HMF. Fig. S30 shows that PO_4-BPL/NiO delivers a higher current at the same potential, confirming that the presence of Cu lowers the OER activity. Moreover, after adding Cu, the oxidation peak potential of Ni^{2+} increases, indicating that Cu helps the oxidation of Ni^{2+} to Ni^{3+}–OOH active sites, which have a significant promoting effect on both HMF electrocatalytic conversion.[53,54]

The intensity of active sites on the electrode surface was assessed by the Differential Pulse Voltammetry Curve (Fig. S31). The Ni peak in the DPV curve is markedly larger, the data show that the amount of active sites participating in the redox reaction increases. The LSV curves in Fig. S30 reveal a larger Ni oxidation peak for PO_4-BPL/CuNiO than for PO_4-BPL/NiO, indicating that Cu modification makes Ni oxidation easier and raises the population of active Ni^{III} species formed *in situ*. To verify the promoting effect of Cu on NiOOH formation, XPS was further employed to observe the overall impact of Cu introduction on the catalyst (Fig. 6f). After Cu was introduced, compared with PO_4-BPL/NiO, the XPS results of PO_4-BPL/CuNiO showed that the peaks of Ni^{2+} and Ni^{3+} shifted to the higher energy side by 0.47 eV and 0.58 eV, respectively. Due to the relatively low electronegativity of Cu, it is more likely to accept electrons, thereby reducing the electron cloud density of Ni atoms and causing electron transfer from Ni atoms to Cu atoms.[19,55] This indicates that the introduction of Cu changed the active sites of Ni atoms and promoted the conversion of Ni between different valence states. Meanwhile, the reduced surface charge density of Ni may also enhance the adsorption ability of Ni atoms to HMF, thereby improving the catalyst's activity. The d-band center and partial densities of states of PO_4-BPL/NiO and PO_4-BPL/CuNiO were also calculated. The d-band center of PO_4-BPL/CuNiO (−1.98 eV) was closer to the Fermi level than PO_4-BPL/NiO (Fig. S32). It indicates that Cu doping lowers the filling of antibonding states at Ni sites, strengthens metal-adsorbate bonding, and reduces

Published on 21 November 2025. Downloaded on 5/17/2026 11:33:50 AM.

the activation energy for adsorption/activation, thereby promoting HMF adsorption.

3.5 DFT calculation of H transfer

Combining theoretical calculations and experimental results, the concept of PO_4-BPL was concretized. Without PO_4-BPL on the surface of CuNiO, the H^+ generated from HMF electro-oxidative dehydrogenation and pre-oxidation could not be transferred rapidly, generating an accumulation of H^+, which could damage the catalyst structure (Fig. 7a and b). The experimental results show that the PO_4-BPL on the surface of PO_4-BPL/CuNiO catalyst can not only promote the transformation of HMF, but also significantly improve the cycling stability. PO_4 forms a rapid proton transfer channel on the catalyst surface, facilitating the PCET process while creating a protective layer. This prevents active H protons generated during the reaction from further penetrating the catalyst's interior and eroding its structure, thereby enhancing stability (Fig. 7c and d).

DFT calculations reveals the adsorption free energy of HMF on CuNiO and PO_4-BPL/CuNiO surfaces. First, the structure of CuNiOOH and PO_4-BPL/CuNiOOH obtained by *in situ* reconstruction of CuNiO and PO_4-BPL/CuNiO was optimized (Fig. S33). Then one molecule of HMF is analytically adsorbed on its surface, the adsorption models and free energies of HMF on CuNiO and PO_4-BPL/CuNiO are presented in Fig. S34 and S35. As shown in Fig. S36, the adsorption energies of HMF on PO_4-BPL/CuNiO and CuNiO were −1.46 and −1.33 eV, respectively, indicating that the PO_4 protective layer on the surface promotes HMF adsorption. This stronger adsorption allows HMF to be stably anchored on the catalyst surface,

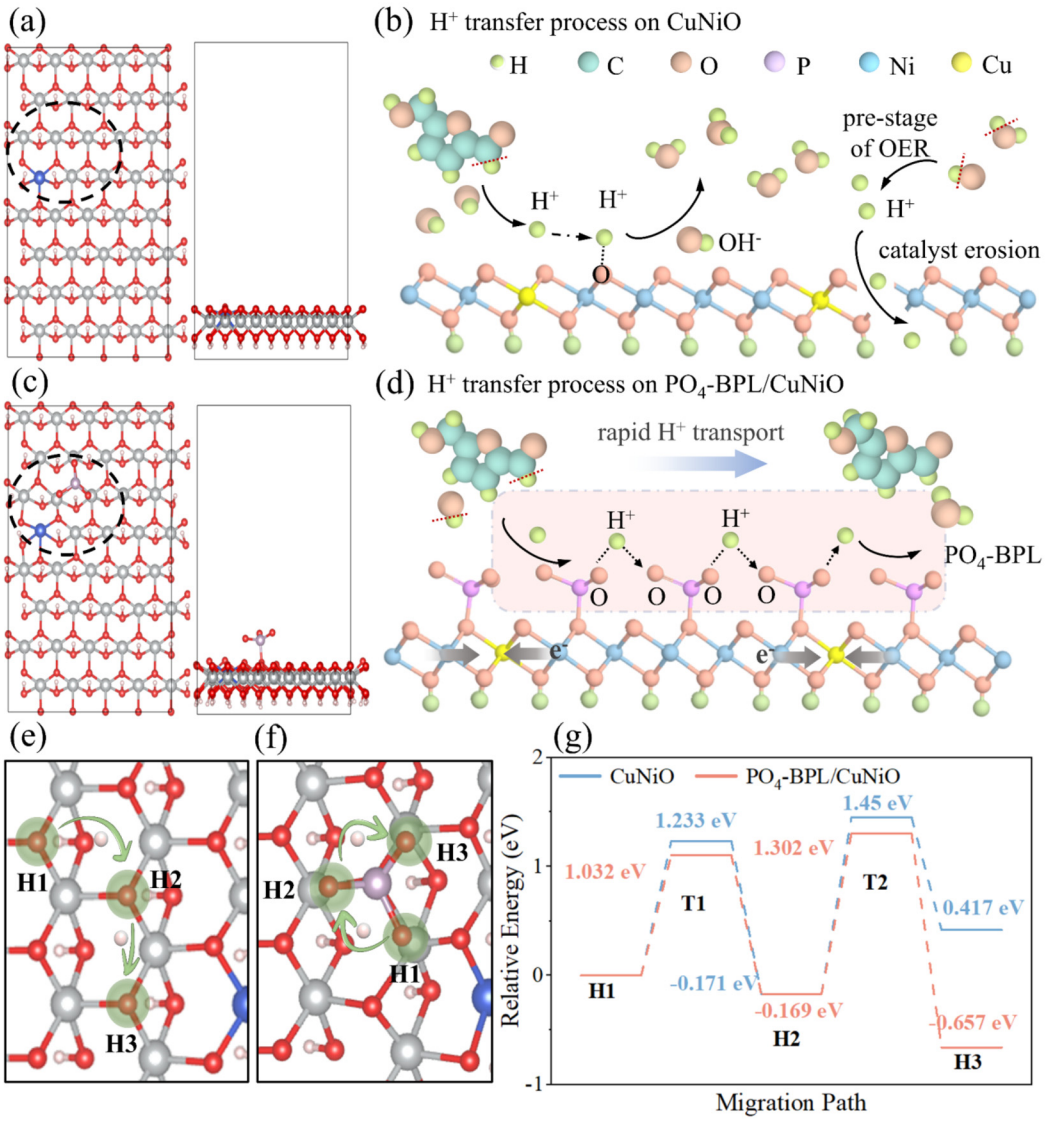

Fig. 7 The top and side view of optimized model of (a) CuNiO and (c) PO_4-BPL/CuNiO. (b) H^+ transfer processes on the surface of CuNiO catalysts. (d) H^+ transfer processes on the surface of PO_4-BPL/CuNiO catalysts. The proposed migration path of H on the electrode surface (e) CuNiO and (f) PO_4-BPL/CuNiO. (g) activation energy required for H proton migration at the H1–H3 site.

 This journal is © The Royal Society of Chemistry 2026

Published on 21 November 2025. Downloaded on 5/17/2026 11:33:50 AM.

reduces the activation energy of the oxidation reaction, and thereby enhances the reaction rate.

The electrocatalytic conversion of HMF to FDCA involves the transfer of H protons from the aldehyde and alcohol hydroxyl groups of HMF to the catalyst surface. Fig. 7e and f illustrate the H migration pathways on the PO_4-BPL/CuNiO surface (at the PO_4 group) and on the CuNiO catalyst surface. DFT calculations of the migration energies and transition state barriers for H protons at sites H1, H2, and H3 enable evaluation of H migration difficulty on the catalyst surface. The adsorption configurations obtained for PO_4-BPL/CuNiO and CuNiO at each site are shown in Fig. S37 and S38, respectively, and the results of the transition state for H proton migration calculated finally are shown in Fig. 7g, during H migration from H1 to H2, the energy barrier for H proton migration on PO_4-BPL/CuNiO was 1.10 eV, compared to 1.23 eV on CuNiO. Similarly, during H migration from H2 to H3, the barrier on PO_4-BPL/CuNiO (1.30 eV) was lower than on CuNiO (1.45 eV). These results indicate that PO_4 reduces the H migration energy on the catalyst surface, enhancing H proton mobility *via* the PO_4 protective layer.

Adsorption energy comparisons for H protons at H1, H2, and H3 further support this conclusion. For PO_4-BPL/CuNiO, the adsorption energies of H protons at H2 and H3 were −0.17 eV and −0.66 eV, respectively, indicating spontaneous H migration within the PO_4 layer. In contrast, for CuNiO, the adsorption energies at H2 and H3 were −0.17 eV and 0.42 eV, suggesting restricted H proton transport and reduced mobility on the bare CuNiO surface. The PO_4 protective layer preferentially binds H protons spontaneously, preventing their further penetration and potential catalyst corrosion.

4. Conclusion

The core green advancement of this work lies in the innovative catalyst design, where inspired by biological phosphate buffer systems, we developed a PO_4-BPL/CuNiO catalyst, creating a buffered microenvironment for stable electrodes. Unlike conventional studies that incorporate complex organic ligands or toxic components, this inherently safe design uses only environmentally friendly phosphate ions, fundamentally adhering to green chemistry principles. The PO_4-BPL enables rapid proton transfer, minimizing H^+ accumulation and preventing catalyst corrosion from localized over acidity. This proton transfer mechanism significantly enhances the electrocatalytic oxidation of HMF. Our bioinspired catalyst achieves a large current density exceeding 700 mA cm^{-2} in the HMF system, with FDCA selectivity surpassing 95%. Notably, the PO_4-BPL/CuNiO catalyst delivers a 7 fold longer cycling life and maintains stable operation for 70 h in a continuous-flow electrolyzer, compared with only 6 h for the catalyst without PO_4-BPL. Using *in situ* Raman spectroscopy and *in situ* electrochemical impedance spectroscopy combined with DRT analysis, we demonstrated the PO_4-BPL's accelerated mass transfer. DFT calculations further revealed the mass transfer acceleration and surface buffering effects of the PO_4-BPL. This work introduces a novel catalyst design strategy for electrocatalytic HMF conversion to FDCA, highlighting the exceptional performance of bioinspired electrocatalysts and offering a promising approach for stable industrial-scale operation.

Author contributions

Wei Ji was responsible for investigation, methodology, writing the original draft, and reviewing and editing the manuscript. Wenjie Zhang contributed to data curation and theoretical calculation. Chen Deng handled conceptualization, methodology and supervision. Yuwei Xiong contributed to methodology, reviewing and data curation. Qi Hao and Hao Zhang participated in reviewing, conceptualization and supervision. Bing Song assisted with the experiments and reviewing and editing the manuscript. Wenlei Zhu and Dekui Shen contributed to methodology and supervision. Jason Chun-Ho Lam provided supervision, reviewing and editing the manuscript. Richen Lin contributed through supervision, funding acquisition, project administration, and reviewing and editing the manuscript.

Conflicts of interest

The authors declare no conflict of interest.

Data availability

The data that support the findings of this study are available from the corresponding author upon reasonable request. The Supplementary Information includes detailed experimental procedures, additional catalyst characterization data, supplementary electrochemical measurements, and computational details.

See DOI: https://doi.org/10.1039/d5gc04249f.

Acknowledgements

This work was supported by Jiangsu Provincial Department of Science and Technology (BZ2024054), the National Natural Science Foundation of China (52276177, 52376172), the State Key Laboratory of Clean Energy Utilization (Open Fund Project No. ZJUCEU2023008), and the Natural Science Foundation of Jiangsu Province (BK20241315). The authors thank the Big Data Computing Center of Southeast University and the Center for Fundamental and Interdisciplinary Sciences of Southeast University. C. Deng acknowledges the Horizon Europe Guarantee MSCA Postdoctoral Fellowship (No. 101153313) funded by the UKRI Engineering and Physical Sciences Research Council (Ref: EP/Z002753/1).

Published on 21 November 2025. Downloaded on 5/17/2026 11:33:50 AM.

References

1 J. Li, R. Qiu, S. Zhang, L. Peng, Y. Dong, Y. Jiang, Y. Li, N. Fang, J. Yu, J. C. Dong, H. Zheng, L. Ding, J. Wan, I. Akpinar, J. Kuang, G. Chen, J. Ye, Y. Sun, L. Lin, S. Zheng, S. Yang, J. Li and J. F. Li, *Adv. Mater.*, 2025, **37**, 2417684.
2 P. Giri, S. Lim, T. P. Khobragade, A. D. Pagar, M. D. Patil, S. Sarak, H. Jeon, S. Joo, Y. Goh, S. Jung, Y.-J. Jang, S. B. Choi, Y. C. Kim, T. J. Kang, Y.-S. Heo and H. Yun, *Nat. Commun.*, 2024, **15**, 6371.
3 Q. Li, D. Gunawan, L. Jiang, R. Gunawan, G. Gunasekara, S. Sarmin, R. Doyle, Q. Lai, R. Amal and J. Scott, *ACS Appl. Eng. Mater.*, 2025, **3**, 21–43.
4 J. Zhang, D. Yan, G. Ding, X. Wang, C. Li, S. Zhong, Y. Yu, L. Shuai and G. Liao, *Angew. Chem., Int. Ed.*, 2025, **64**, e202511448.
5 Y. Gao, L. Ge, H. Xu, K. Davey, Y. Zheng and S.-Z. Qiao, *ACS Catal.*, 2023, **13**, 11204–11231.
6 Y. Shen, H. Deng, Y. C. Huang, P. Du, H. Zhou, M. Ma, A. Shen, M. Wang, C. L. Dong, L. Xu and S. Shen, *Adv. Energy Mater.*, 2024, 2405364.
7 S. Li, X. Sun, Z. Yao, X. Zhong, Y. Cao, Y. Liang, Z. Wei, S. Deng, G. Zhuang, X. Li and J. Wang, *Adv. Funct. Mater.*, 2019, **29**, 1904780.
8 M. Sajid, X. Zhao and D. Liu, *Green Chem.*, 2018, **20**, 5427–5453.
9 C. Chen, L. Wang, B. Zhu, Z. Zhou, S. I. El-Hout, J. Yang and J. Zhang, *J. Energy Chem.*, 2021, **54**, 528–554.
10 X.-L. Li, R. Zhu and H.-J. Xu, *ACS Sustainable Chem. Eng.*, 2025, **13**(6), 2223–2259.
11 Y. Liu, Z. Yang, Y. Zou, S. Wang and J. He, *Small*, 2024, **20**, e2306488.
12 J. Wang, W. Zhao, Z. Zhao, H. Yu, W. Wang, Y. Xu, X. Liu, L.-L. Shen, G.-R. Zhang and D. Mei, *Appl. Catal., B*, 2025, **371**, 125229.
13 M. Li, S. Hu, Y. Zhang, J. Qin, D. Min, C. Chen, P. Zhang, L. Jiang and J. Zhang, *Appl. Catal., B*, 2025, **368**, 125130.
14 L. Zhang, Y. Liu, L. Li, T. Wu, Q. Wu, J. Z. Y. Seow, X. Lin, S. Sun, L. Tannesia, K. Tang, D. Shao, S. Xi, X. Guo and Z. J. Xu, *Energy Environ. Sci.*, 2025, **18**, 5622–5631.
15 L. Chico-Mesa, A. Rodes, R. M. Arán-Ais and E. Herrero, *Nat. Commun.*, 2025, **16**, 3349.
16 X. Huang, O. Akdim, M. Douthwaite, K. Wang, L. Zhao, R. J. Lewis, S. Pattisson, I. T. Daniel, P. J. Miedziak, G. Shaw, D. J. Morgan, S. M. Althahban, T. E. Davies, Q. He, F. Wang, J. Fu, D. Bethell, S. McIntosh, C. J. Kiely and G. J. Hutchings, *Nature*, 2022, **603**, 271–275.
17 F. Ma, C. Zhang, W. Li, R. Hu, Z. Wang, J. Wang, J. Li, Y. Nie, Z. Zheng and X. Jiang, *ACS Catal.*, 2025, **15**, 4759–4769.
18 B. Liu, Z. Zheng, Y. Liu, M. Zhang, Y. Wang, Y. Wan and K. Yan, *J. Energy Chem.*, 2023, **78**, 412–421.
19 J. Wu, Z. Zhai, T. Yu, X. Wu, S. Huang, W. Cao, Y. Jiang, J. Pei and S. Yin, *J. Energy Chem.*, 2023, **86**, 480–489.
20 C. Liu, X. R. Shi, K. Yue, P. Wang, K. Zhan, X. Wang, B. Y. Xia and Y. Yan, *Adv. Mater.*, 2023, **35**, e2211177.
21 Y. Chen, J. Qiu, S. Li, J. Zhang, Y. Liu, X. Chen, X. Liu, S. Dou and D. Wang, *Adv. Funct. Mater.*, 2024, **35**, 2414587.
22 D. Chen, W. Li, J. Liu and L. Sun, *Energy Environ. Sci.*, 2025, **18**, 3120–3128.
23 B. Gao, X. Mu, J. Feng, H. Huang, J. Liu, W. Liu, Z. Zou and Z. Li, *Angew. Chem., Int. Ed.*, 2024, **64**, e202413298.
24 J. Woo, J. Choi, J. Choi, M. Y. Lee, E. Kim, S. Yun, S. Yoo, E. Lee, U. Lee, D. H. Won, J. H. Park, Y. J. Hwang, J. S. Yoo and D. K. Lee, *Adv. Funct. Mater.*, 2024, **35**, 2413951.
25 J. Qi, Q. Chen, M. Chen, W. Zhang, X. Shen, J. Li, E. Shangguan and R. Cao, *Small*, 2024, **20**, e2403310.
26 H. Liao, T. Luo, P. Tan, K. Chen, L. Lu, Y. Liu, M. Liu and J. Pan, *Adv. Funct. Mater.*, 2021, **31**, 2102772.
27 J. Jin, J. Yin, Y. Hu, Y. Zheng, H. Liu, X. Wang, P. Xi and C. H. Yan, *Angew. Chem., Int. Ed.*, 2024, **63**, e202313185.
28 M. Han, H. Wang, J. Zhou, K. Liu, N. Wang, X. Chen, Y. Liu and H. Liang, *Adv. Funct. Mater.*, 2024, **35**, 2415143.
29 Z. Xia, L. Xu, C. Ma, Q. An, C. Bu, Y. Fan, Y. Lu, Y. Pan, D. Xie, Q. Liu, S. Wang and Y. Zou, *J. Am. Chem. Soc.*, 2024, **146**, 24570–24579.
30 Y. Wang, Q. Lu, X. Ge, F. Li, L. Chen, Z. Zhang, Z. Fu, Y. Lu, Y. Song and Y. Bu, *Green Energy Environ.*, 2024, **9**, 344–355.
31 X. Gao, Y. Zhu, S. Yang, W. Zhang and R. Cao, *J. Energy Chem.*, 2025, **103**, 393–399.
32 Y.-N. Zhou, N. Yu, R.-Y. Fan, M. Hojamberdiev, H. Hu, B. Dong, Y.-M. Chai and Q. Tang, *Appl. Catal., B*, 2025, **361**, 124692.
33 H. Liu, J. Zhang, X. Li, R. Zhang, W. Jia, J. Zhang, Y. Sun and L. Peng, *Appl. Catal., B*, 2025, **365**, 124994.
34 D.-H. Nam, B. J. Taitt and K.-S. Choi, *ACS Catal.*, 2018, **8**, 1197–1206.
35 D. Chen, Y. Ding, X. Cao, L. Wang, H. Lee, G. Lin, W. Li, G. Ding and L. Sun, *Angew. Chem., Int. Ed.*, 2023, **62**, e202309478.
36 T. H. Wan, M. Saccoccio, C. Chen and F. Ciucci, *Electrochim. Acta*, 2015, **184**, 483–499.
37 F. Ciucci and C. Chen, *Electrochim. Acta*, 2015, **167**, 439–454.
38 Y. Sun, J. Wang, Y. Qi, W. Li and C. Wang, *Adv. Sci.*, 2022, **9**, e2200957.
39 R. Zhang, F. Gao, C. Yang, Y. Bian, G. Wang, K. Xue, J. Zhang, C. Wang and X. Gao, *Mater. Today Nano*, 2023, **23**, 100373.
40 Y. Jia, Z. Gui, W. Zhang, T. Yan, J. Tan, L. Chen, Q. Gao, Y. Zhang and Y. Tang, *ACS Appl. Mater. Interfaces*, 2024, **16**, 8697–8706.
41 L. Zhang, J. Liang, Y. Wang, T. Mou, Y. Lin, L. Yue, T. Li, Q. Liu, Y. Luo, N. Li, B. Tang, Y. Liu, S. Gao, A. A. Alshehri, X. Guo, D. Ma and X. Sun, *Angew. Chem., Int. Ed.*, 2021, **60**, 25263–25268.
42 H. Wang, Y. Zhou and S. Tao, *Appl. Catal., B*, 2022, **315**, 121588.
43 D. Wang, Z. Liu, Y. Qiao, Z. Jiang, P. Zhu, J. Zeng, W. Peng, Q. Lian, G. Qu, Y. Xu, Y. Zhang, F. Li, L. Yan, X. Wang, Y.-G. Wang, A. K. Y. Jen and B. Xu, *Joule*, 2025, **9**, 101815.
44 H. N. Pollen, I.-E. Nylund, Ø. Dahl, A. M. Svensson, D. Brandell, R. Younesi, J. R. Tolchard and N. P. Wagner, *ACS Appl. Energy Mater.*, 2023, **6**, 12032–12042.

 This journal is © The Royal Society of Chemistry 2026

45 X. Jiang, W. Li, Y. Liu, L. Zhao, Z. Chen, L. Zhang, Y. Zhang and S. Yun, *SusMat*, 2023, **3**, 21–43.
46 Y. Yang and T. Mu, *Green Chem.*, 2021, **23**, 4228–4254.
47 L. Guo, X. Zhang, L. Gan, L. Pan, C. Shi, Z. F. Huang, X. Zhang and J. J. Zou, *Adv. Sci.*, 2023, **10**, e2205540.
48 Z. Yang, L. Chen, Y. Yin, C. Wei, Z. Xue and T. Mu, *Energy Environ. Sci.*, 2024, **17**, 8801–8809.
49 J. Kim, T. Begildayeva, J. Theerthagiri, C. J. Moon, A. Min, S. J. Lee, G.-A. Kim and M. Y. Choi, *J. Energy Chem.*, 2023, **84**, 50–61.
50 J. Zhang, J. Wei, Z. Zhai, H. Wen, B. Feng, X. Wu, D. Meng, J. Wu and S. Yin, *Appl. Catal., B*, 2025, **373**, 125331.
51 S. Li, S. Wang, Y. Wang, J. He, K. Li, Y. Xu, M. Wang, S. Zhao, X. Li, X. Zhong and J. Wang, *Adv. Funct. Mater.*, 2023, **33**, 2214488.
52 M. Zubair, P. M. Usov, H. Ohtsu, J. A. Yuwono, C. S. Gerke, G. D. Y. Foley, H. Hackbarth, R. F. Webster, Y. Yang, W. H. Lie, Z. Ma, L. Thomsen, M. Kawano and N. M. Bedford, *Adv. Energy Mater.*, 2024, **14**, 2400676.
53 X. Li, W. Zhu, F. Yue, H. Pang, C. Wang, D. Wang, Y. Lu and C. Yang, *Appl. Catal., B*, 2024, **358**, 124418.
54 P. Hauke, T. Merzdorf, M. Klingenhof and P. Strasser, *Nat. Commun.*, 2023, **14**, 4708.
55 H. Xu, G. Xin, W. Hu, Z. Zhang, C. Si, J. Chen, L. Lu, Y. Peng and X. Li, *Appl. Catal., B*, 2023, **339**, 123157.

Published on 21 November 2025. Downloaded on 5/17/2026 11:33:50 AM.